Electrochimica Acta 439 (2023) 141599

Contents lists available at ScienceDirect

Electrochimica Acta

journal homepage: www.journals.elsevier.com/electrochimica-acta

Hierarchical SnO_2@PC@PANI composite *via in-situ* polymerization towards next-generation Li-ion capacitor by limiting alloying process with high energy, wide temperature performance, and cyclability

Manohar Akshay [a], Selvarasu Praneetha [a], Yun-Sung Lee [b,*], Vanchiappan Aravindan [a,*]

[a] Department of Chemistry, Indian Institute of Science Education and Research (IISER) Tirupati 517507, India
[b] School of Chemical Engineering, Chonnam National University, Gwang-ju 61186, Republic of Korea

ARTICLE INFO

Keywords:
Li-ion capacitor
Alloy-anode
In-situ polymerization
In-situ impedance
Energy density

ABSTRACT

Lithium-ion capacitors (LICs) are promising electrochemical energy storage devices with hybridization of the battery-type anode and capacitive-type cathode, bringing high energy density and high power density simultaneously in a single device. We report the extraction of activated carbon from the palmyra fruit, *in-situ* polymerization with polyaniline (PANI), and the making of different composite formulations with SnO_2 to be used as anode for LIC with palmyra fruit-derived activated carbon (PC) as the cathode. The SnO_2@PC@PANI electrode is restricted to 1 V *vs.* Li, which allows only the alloying reaction and eliminates the conversion process. An *in-situ* impedance study is performed to validate the formation and depletion of the solid electrolyte interface over the battery-type electrode upon cycling. Prior to the fabrication of the LIC, the SnO_2@PC@PANI is electrochemically pre-lithiated. The fabricated LIC with balanced mass loadings exhibits a mesmerizing electrochemical performance with a maximum energy density of ~175 Wh kg^{-1} at room temperature. The possibility of LIC in different climatic conditions is also analyzed by testing its electrochemical performance in different temperature conditions.

1. Introduction

Greenhouse gas emission is increasing tremendously due to increased fossil fuel consumption, escalating global warming, and other environmental impacts [1]. In this context, innovative steps should be taken to reduce its effect on the environment by exploring alternative renewable energy sources. We have different clean, renewable, and environmentally friendly energy sources such as solar, wind, tidal, etc. However, the storage of these forms of energy is a big challenge. Electrochemical energy storage is the most promising among the different energy storage devices. Since Sony commercialized the first Lithium-ion battery (LIB) in 1991, the research on batteries has increased exponentially to improve their performance. They have been significantly explored and are used in several electrical devices, including mobile phones, laptops, medical applications, etc. However, they still lack the power density required for high-end applications. Meanwhile, electrical double-layer capacitors (EDLCs) have a high power density but decreased energy density. In this context, there came the necessity for a single device with energy and power density. Hence, there arose the idea of Lithium-ion capacitors (LICs).

LIC is a hybrid supercapacitor that consists of a battery-type (faradaic reaction) anode paired with a capacitive-type (non-faradaic reaction) cathode. This hybrid device has a higher energy density than EDLCs and a high power density than LIBs. Hence, they can bridge the gap between EDLCs and LIBs [2–6]. The performance of LICs majorly depends on the battery type electrode, *i.e.*, anode. Therefore, most of the research activities in LICs are carried out on battery-type electrodes [7–14]. The exploration started with the insertion type [15] electrodes such as $Li_4Ti_5O_{12}$, graphite, etc. However, the lack of energy density for these insertion anodes makes people think of high-capacity alloying and conversion anodes [5,16–20]. The theoretical capacities of alloy/conversion-type anodes are more than (>600 mAh g^{-1}) that of the abovementioned insertion types [21]. Moreover, the operational potentials are moderate and have good safety characteristics. Among the different electrode materials, SnO_2 is one of the guaranteed candidates due to its high theoretical capacity (>750 mAh g^{-1}), abundance, and lower redox potential (~0.3 V *vs.* Li) [22–25]. Nevertheless, one of the main challenges to overcome is the volume variation (up to 300%)

* Corresponding authors.
E-mail addresses: leeys@chonnam.ac.kr (Y.-S. Lee), aravind_van@yahoo.com (V. Aravindan).

https://doi.org/10.1016/j.electacta.2022.141599
Received 15 October 2022; Received in revised form 12 November 2022; Accepted 22 November 2022
Available online 23 November 2022

caused during cycling, which could lead to the instability of the cell. Many research efforts are being reported in which morphology-controlled nanoparticles are synthesized at various dimensions to alleviate the pulverization of electrodes during cycling [26–30]. In our work, we synthesized hierarchical flower-shaped SnO_2 nanostructures by a simple hydrothermal method and utilized them as anodes for LIC applications. The stability is improved by hybridizing with palmyra fruit-derived activated carbon (PC) and *in-situ* polymerized polyaniline (PANI). The polymer PANI enhanced the conductivity and flexibility of the SnO_2 electrode by stabilizing its volume variation and thereby provided better stability [31]. Mass loading between the battery and capacitive-type electrodes was optimized based on the half-cell performance (*vs*. Li) and subsequently pre-lithiated prior to the fabrication of the LIC. The better electrochemical performance was exhibited by both half-cell, and full-cell configurations with superior energy density, power density, and long-term cyclic stability even at different temperature conditions are discussed in detail. Moreover, while comparing with previously reported SnO_2-based LICs, our AC/S-nO_2@PC@PANI LIC exhibits superior performance in terms of energy and power density [32–36].

2. Experimental section

2.1. Material preparation

Synthesis of Urchin structured SnO_2: $SnCl_2.2H_2O$ and NaOH were selected as starting materials. All the reagents purchased from Sigma-Aldrich were of analytical grade and needed no further purifications. 6 mM $SnCl_2{\cdot}2H_2O$ was dissolved into 15 mL water and 5 mL ethanol. Then 0.4 mol L^{-1} NaOH solution was dropped into $SnCl_2$ solution until pH=13 under continuous magnetic stirring. The obtained mixture was transferred into a 100 mL Teflon-lined stainless-steel autoclave, sealed and maintained at 180 °C for 24 h, and then cooled to room temperature. The precipitate was centrifuged and washed several times with water and ethanol, respectively, until Cl^- ions could not be detected. The products were finally dried in the vacuum at 75 °C for 1 h.

Extraction of Activated Carbon from Asian Palmyra Fruit and its in-situ Polymerization: The activated carbon (PC) was prepared from palmyra fruit *Borassus species, B. flabellifer* (Asian Palm tree) is dioecious with male and female flowers on separate plants. After pollination, the bloomed female flowers become fleshy fruits. Then the fruits turned from black to brown with sweet, fibrous soft orange-yellow pulp was taken out, and the sun-dried and minced mixture underwent a carbonization process at 350 °C for 2 h. The activated carbon was prepared by chemical activation with KOH. The ratio between the carbon sample to KOH is 1:0.1 wt.% in 100 mL of deionized water for 12 h at 60 °C. The black solution is allowed to dry in an air oven before pyrolysis in a tubular furnace at 900 °C for 2 h under an Argon atmosphere (Scheme 1). The resulting sample is washed with 2 N HCl to remove K^+ ions, followed by several washing until pH reaches 7. Thus, the PC sample was allowed to dry at 90 °C overnight and collected and stored for further characterization.

In-situ Polymerization of Palmyra fruit Carbon/Polyaniline: For nitric acid treatment of prepared PC, the first 1 g of raw PC powder and 50 mL of 1 M HNO_3 solution were stirred using a magnetic stirrer for 3 h at 90 °C. After cooling to room temperature, the PC powder was filtered and washed with distilled water several times until pH increased to a neutral value; the oxidized PC was then dried in the vacuum drying oven at 100 °C for 4 h (Surface area: 985.7 $m^2\ g^{-1}$ and Pore volume: 0.709 cc g^{-1}, Fig. S1).

For *in-situ* polymerization, 1 g of PC and 0.4 g of sodium lauryl sulfate (SLS) were dissolved in 40 mL of 1 M H_2SO_4, stirred for 30 min., and mixed. 1 mL of aniline monomer was added to the mixture under stirring. Then 1 g APS as an oxidant was dissolved in 20 ml of 1 M H_2SO_4 and added dropwise to the reaction mixture under vigorous stirring. The reaction vessel was placed in an ice bath during the addition of the oxidant. The reaction mixture was left stirring for about 3 h at a low temperature (0–5 °C). Consequently, the precipitated polymer was

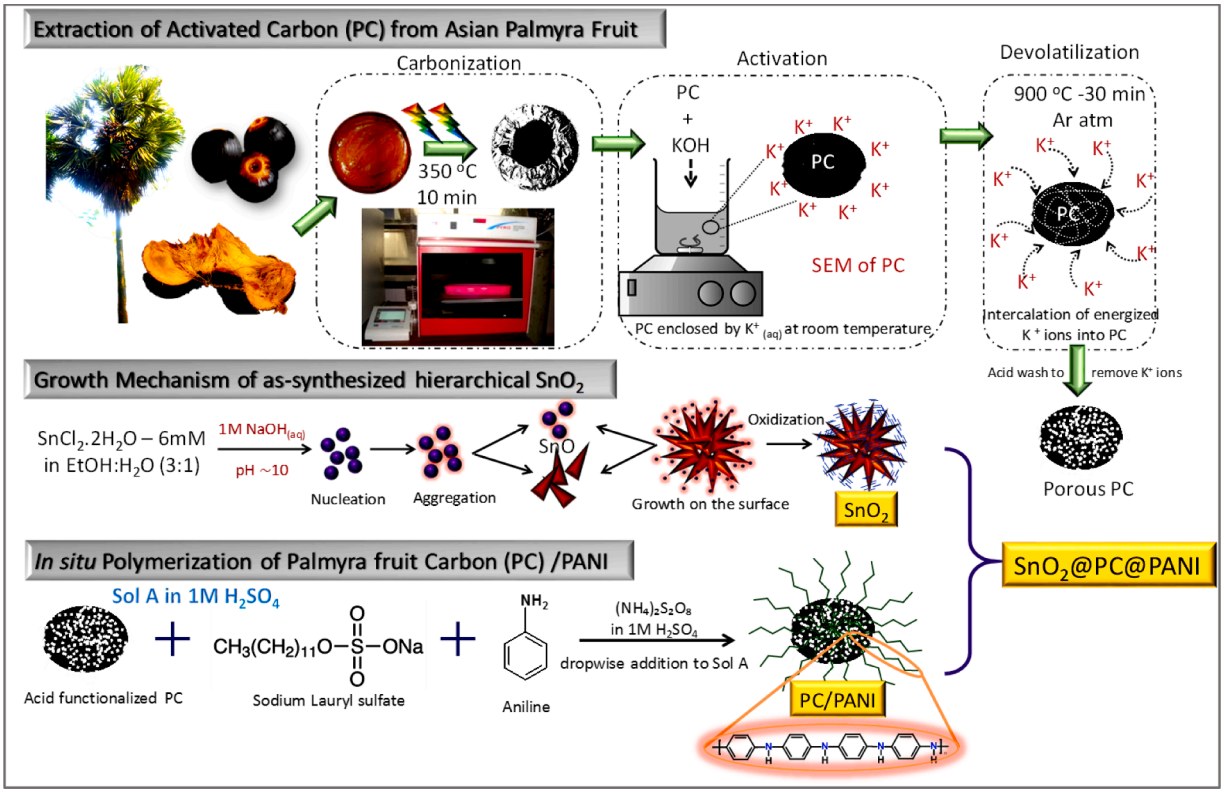

Scheme 1. Schematic representation of the preparation of the SnO_2@PC@PANI composite.

filtered and washed with ethanol and distilled water to remove oligomers and other non-polymeric impurities until the washing liquid was colourless. The polymer was dried in a vacuum oven at 60 °C for 24 h. The activated carbon/ polyaniline composite (PC–PANI) was synthesized using the procedure above without SLS addition and at a polymerization temperature of 25 °C. *In-situ* polymerization and proposed composite interaction are schematically illustrated below.

Material characterization: The phase and purity of the synthesized SnO_2 nanoparticles were examined using powder X-ray diffraction (XRD) measurement (Rigaku D/teX Ultra 250 diffractometer; 40 kV, 200 mA, $\lambda = 1.5406$ Å with Cu Kα radiation). Raman spectroscopy analysis was carried out by Lab Ram HR800 UV Raman microscope (Horiba Jobin-Yvon, France). The morphological analysis and internal structure of the synthesized SnO_2 nanoparticle were performed using a Field-emission scanning electron microscope (FE-SEM S-4700, Hitachi, Japan) and the High-resolution transmission electron microscope (HR-TEM, TECNAI, Philips, the Netherlands, 200 keV), respectively. Further analysis of the elemental composition and surface functional groups was performed using X-ray photoelectron spectroscopy (XPS, Multilab 2000, UK; monochromatic Al Kα radiation $h\nu = 1486.6$ eV), High angle annular dark-field imaging (HAADF) detector and Energy-dispersive X-ray spectroscopy (EDS).

Electrochemical analysis: The SnO_2@PC@PANI electrodes for electrochemical analysis were fabricated using the conventional slurry coating method. Firstly, hydrothermally synthesized SnO_2 nanostructures were mixed with a previously prepared PC-PANI mixture in the ratio of 50:25:25 (SnO_2@PC@PANI). The electrode slurry is then prepared by mixing the 80% active material (SnO_2@PC@PANI) with 10% conductive carbon (acetylene black) and 10% binder (polyvinylidene fluoride, PVdF) in N-Methyl-2-pyrrolidone (NMP) solvent to form a slurry. This slurry was coated on Cu-foil using a doctor blade apparatus, followed by complete drying at 65 °C overnight. These were then cut into 12 mm diameter electrodes, kept at 75 °C in a vacuum oven, and used in CR2016 coin cells with glass microfiber separators (Whatman, Cat no. 1825–047, UK) with metallic lithium as a counter/ reference electrode. 1 M $LiPF_6$ dissolved in ethylene carbonate (EC) and dimethyl carbonate (DMC) in a 1:1 ratio (Tomiyama, Japan) with 9% Fluoroethylene carbonate (FEC) was the electrolyte used.

The PC electrode was composed of 8 mg of Palm-derived activated carbon, 1 mg of conductive additive (acetylene black), and 1 mg binder (teflonized acetylene black, TAB-2), which were mixed in a mortar pestle with ethanol into a freestanding film. Later, the film was pressed onto a 14 mm diameter stainless steel mesh (Goodfellow, UK), which acted as the current collector. These were kept overnight at 75 °C in a vacuum oven to make the test cells with metallic lithium as a counter/ reference electrode for the half-cell assembly in CR2016 coin cells. Before the balanced full-cell fabrication, the SnO_2@PC@PANI half-cells were subjected to 3 complete cycles of charge-discharge, and the cell was de-crimped to remove the electrode carefully in the discharge (pre-lithiated) state. The mass of active material in the Palm activated carbon electrode was adjusted according to the former's capacity, and full cells were fabricated with a glass microfiber separator. All the half-cells and full-cells were fabricated in an argon-filled glove box (MBraun, Germany) with the oxygen and moisture level at <0.1 ppm. The half cells Li/SnO_2@PC@PANI and Li/AC have tested in the potential window of 0.005 to 1 V and 2 to 4.5 V *vs.* Li, respectively. All the GCD studies, cyclic voltammetry (CV), and the *in-situ*-electrochemical impedance spectroscopy (EIS) of the cells were carried out using the Biologic BCS 805 (France) battery tester. And the temperature-dependent performance of the LIC was analyzed in the environmental chamber (Espec, Japan).

3. Results and discussion

Powder XRD measurements were carried out to analyze the crystalline structure, phase purity, and chemical composition of the synthesized SnO_2 nanoparticles and the SnO_2@PC@PANI composite (Fig. 1

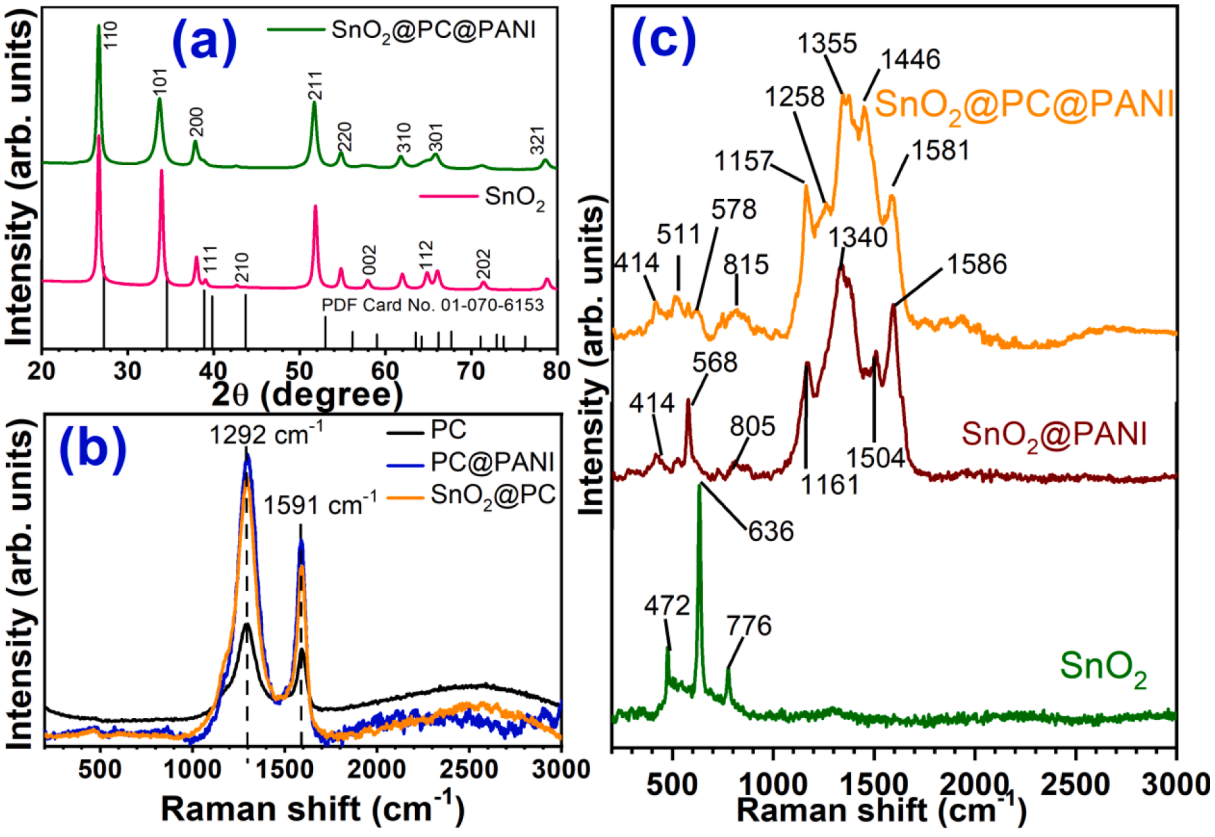

Fig. 1. Physical characterization of SnO_2 and its composites: (a) XRD pattern and (b and c) Raman spectrum.

(a)). The diffraction peaks of SnO_2 correspond to the Cassiterite, syn phase with lattice parameters $a = b = 4.7365$ Å and $c = 3.201$ Å and 136 : *P42/mnm* space group (DB Card Number: 01–070–6153). The diffraction peaks of SnO_2@PC@PANI are also indexed to Cassiterite, syn phase with the same 136 : *P42/mnm* space group with lattice parameters $a = b = 4.7396$ Å and $c = 3.205$ Å (DB Card Number: 01–070–6153). The prominent sharp peak at $2\theta = 26.5°$, 33.8°, and 51.68° correspond to the planes (110), (101), and (211), respectively. The crystallite size was calculated using Scherrer's equation ($D = 0.9\lambda/\beta \cos\theta$) and is found to be 19.5 nm. Fig. 1(b) shows the Raman spectra of the different composites of PC and SnO_2. The PC shows an intense peak at ~1292 cm^{-1} representing the D band (dispersive or defect band) and a less intense G band at ~1591 cm^{-1}. The PC@PANI and SnO_2@PC also show a similar characteristic peak at the same vibration peak representing these two bands. The characteristic Raman peaks of SnO_2, SnO_2@PANI, and SnO_2@PC@PANI are given in Fig. 1(c). For example, the vibrational peaks observed at ~472, ~636, and ~776 cm^{-1} are associated with the E_g, A_{1g} and B_{2g} modes of the SnO_2. Apparently, the E_g mode is related to the vibration of the oxygen atoms in the plane of Oxygen. However, the non-degenerative modes, such as A_{1g} and B_{2g} represent the expansion and contraction of the Sn–O bonds. The three vibrational modes are seen from all the three composites like bare SnO_2, SnO_2@PANI, and SnO_2@PC@PANI, in which the vibration bands are shifted towards the lower wavenumber. This clearly indicates the strong interaction of the SnO_2 with high surface area PC and the conducting polymer, PANI.

The surface chemistry and redox states of the synthesized SnO_2 nanoflower are analyzed using the X-ray photoelectron spectroscopy (XPS) given in Fig. 2. The existence of four elements (Sn, C, O, and N) was confirmed from the survey spectrum. Fig. 2(a) shows the deconvoluted Sn 3d spectra with peaks at ~495.2 and ~486.8 eV corresponding to Sn $3d_{3/2}$ and Sn $3d_{5/2}$, respectively, which confirms the existence of Sn in the 4+ oxidation state [37]. Furthermore, the binding energy of Sn's 3d electron can be obtained from the binding energy difference between Sn $3d_{3/2}$ and Sn $3d_{5/2}$, which further agrees with the standard database [17,38]. The O 1s spectrum (Fig. 2(b)) of oxygen is deconvoluted into three peaks with binding energies values of ~532.2, ~530.7, and ~529.8 eV corresponding to oxygen in O═C, O—C and Sn—O, respectively [39]. The deconvoluted peaks of C 1s (Fig. 2(c)) have three bands positioned at ~285.6, ~284.6, and ~284.4 eV. The spectrum of N 1 s is also given in Fig. 2(d), showing a peak at ~400.3 eV, indicating the presence of the N element at the surface, which originated from the *in-situ* polymerized PANI.

The surface morphological features of SnO_2 were observed using field emission-scanning electron microscopy (FE-SEM). Urchin-like structures are observed from FE-SEM images at different magnifications in Fig. 3(a–e). The plate-like petals are formed as a branch-like structure that is joined together and appears as an urchin-like hierarchical three-dimensional morphology. The formation of such a structure is detailed in the experimental section. Moreover, the size and internal structure of the SnO_2 flowers were analyzed using a high-resolution transmission electron microscope (HR-TEM), given in Fig. 3(f–h). The HR-TEM clearly shows that each petal is nothing but a single crystalline nature of SnO_2 crystals. Such crystallinity is clearly evident from the HR-TEM pictures. The *d*-spacing of lattice fringes was calculated from these HR-TEM images and found to be 0.344 nm. The crystalline nature of SnO_2 was further confirmed by the bright spots of the selected area

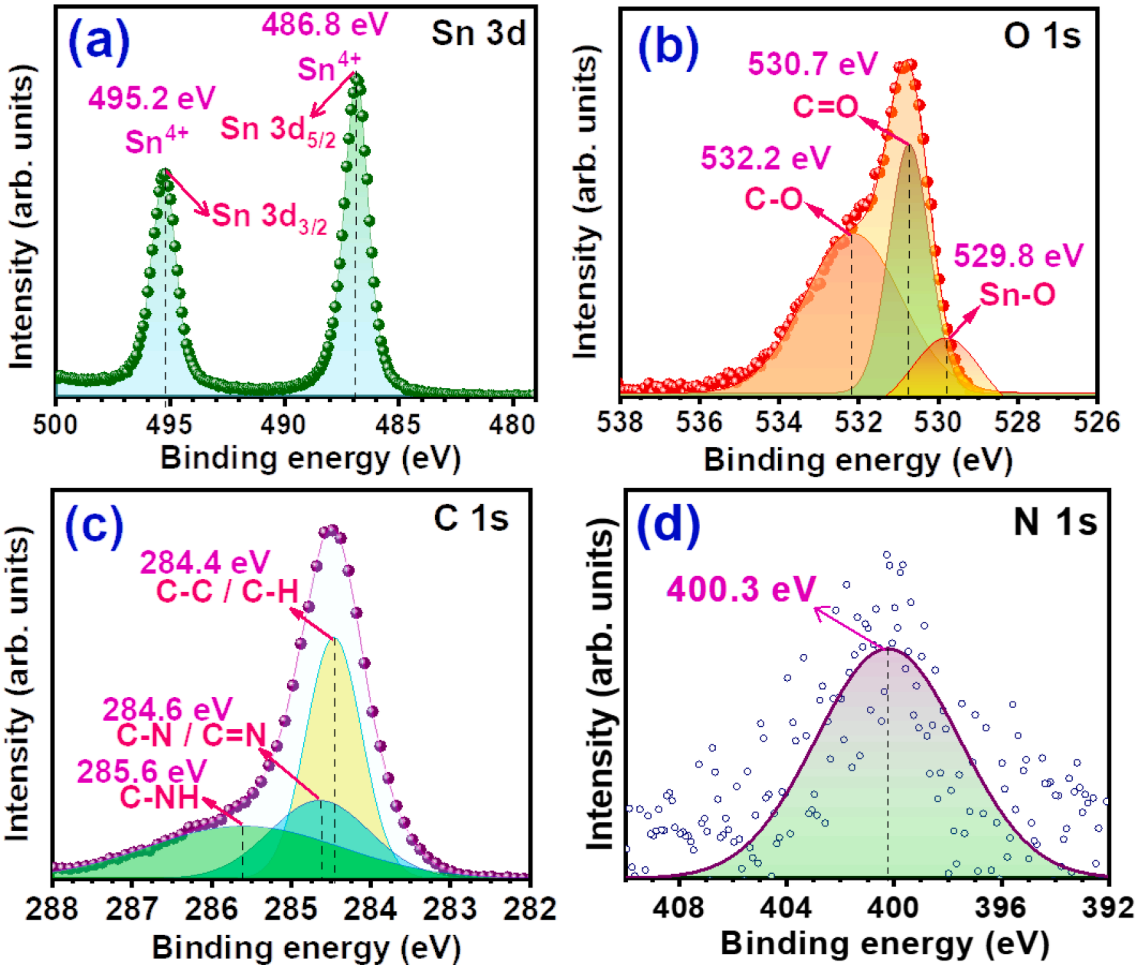

Fig. 2. Deconvoluted XPS spectra of SnO_2: the high-resolution spectrum of (a) Sn 3d, (b) O 1s, (c) C 1s and (d) N 1s.

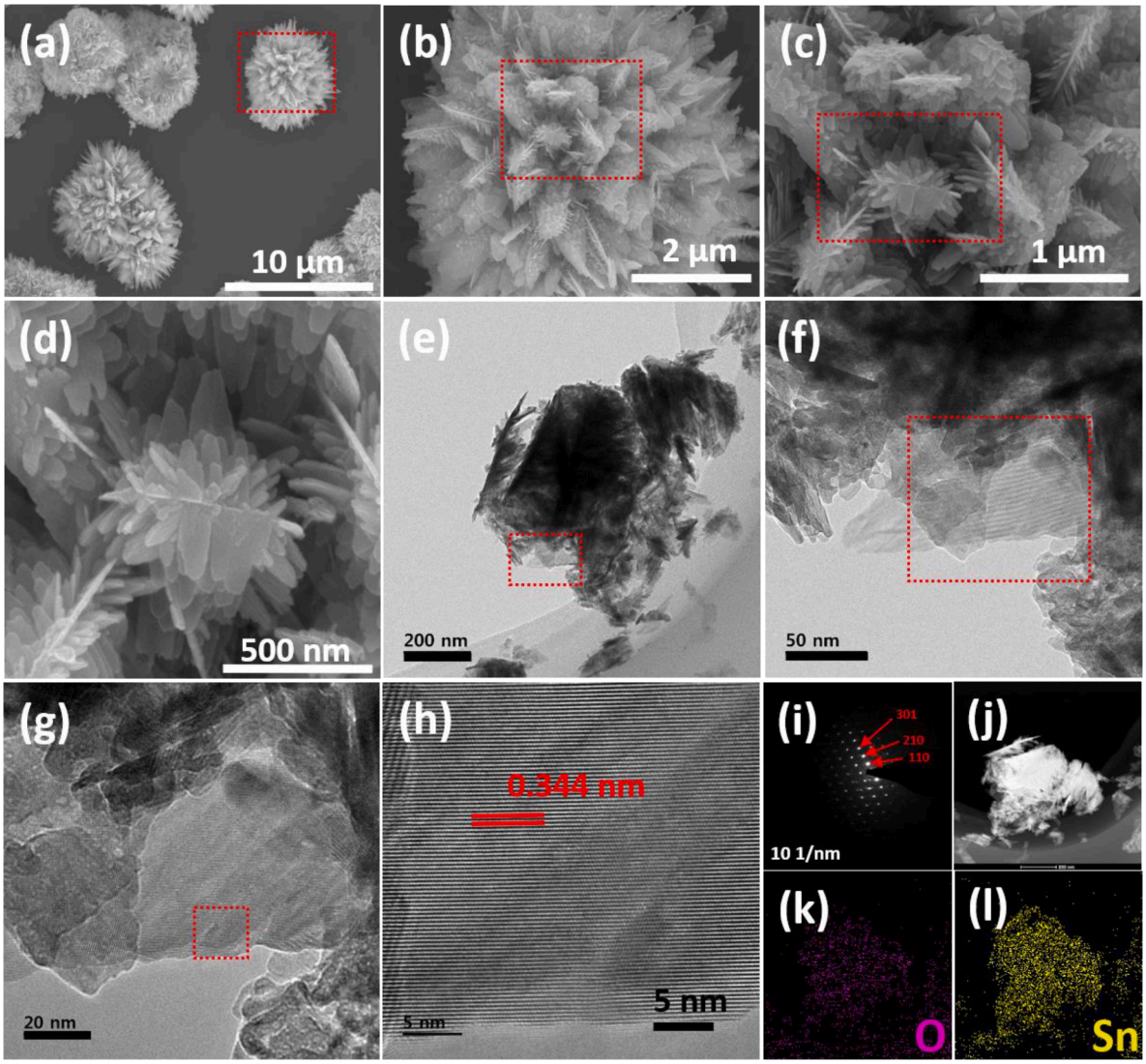

Fig. 3. Microscopic characterization of SnO_2: (a–d) FE-SEM images at different magnifications, (e–h) HR-TEM images, (i) SAED pattern, (j) HAADF-STEM image, and (k and l) EDS mapping.

electron diffraction (SAED) patterns (Fig. 3(i)). Fig. 3(j) displays the STEM image recorded by the HAADF detector, and the elemental distribution was clearly evident from the EDS elemental mapping and is given in Fig. 3(k, l).

3.1. Electrochemical performance

Fig. 4(a) shows a series of cyclic voltammetric (CV) analyses SnO_2@PC@PANI between 0.005 to 1 V *vs.* Li at a scan rate of 0.1 mV s^{-1}. Upon the first cathodic scan, the sharp reduction peak positioned around ~0.8 V *vs.* Li is considered a decomposition of the electrolyte solution and structural destruction of the SnO_2 ($SnO_2 + Li \rightarrow Sn^0 + Li_2O$). The decomposition of the electrolyte leads to the formation of a passivating layer called "solid electrolyte interphase (SEI)" [28]. The SEI layer formation consumes the Li-ions in an irreversible manner and results in huge irreversibility upon anodic scan. The stable SEI layer formation is one of the prime issues for alloy anodes. In general, the SEI will be formed during the cathodic scan (or discharge process), and the depletion of such layer takes place during the anodic scan (or charge process). However, it is worth mentioning that the formation and depletion of the SEI layer are not 100% reversible, which will be validated in the forthcoming *in-situ* impedance measurements. The CV profile of bare SnO_2 (2^{nd} cycle) has a broad cathodic peak observed at ~0.21 V *vs.* Li, indicating the Li_xSn alloy formation ($Sn^0 + Li \rightarrow Li_xSn$) [23]. Conversely, the anodic peak recorded at ~0.5 V *vs.* Li displays the de-alloying reaction, *i.e.,* re-formation of metallic Sn (Sn^0) from Li_xSn alloy ($Li_xSn \rightarrow Sn^0 + Li$). Similar cathodic and anodic peaks can be observed for all the composites indicating alloying/de-alloying reactions with a slight shift in the potential values (Fig. S2).

The galvanostatic charge-discharge analysis (GCD) of the bare SnO_2 and different SnO_2 composites was performed in the potential window of 0.005 to 1 V *vs.* Li at a current rate of 0.1 A g^{-1} (Fig. 4(b, c)). Similar to the CV profile, the presence of a long-distinct plateau observed during the discharge process at ~0.9 V *vs.* Li is associated with structural destruction of SnO_2 and SEI formation. Followed by the plateau, the appearance of the monotonous curves, which is nothing but the formation of the reversible Li_xSn alloy (Fig. S3). The electrochemical event recorded in the first cycle originated from the open circuit potential of the cell, irrespective of either CV or galvanostatic analysis. On the other hand, the test cell is limited to the upper cut-off potential of the 1 V *vs.* Li, which means it allows only the de-alloying process, not for oxidation of the metallic Sn^0 into Sn^{2+} (SnO) or Sn^{4+} (SnO_2), *i.e.*, conversion reaction. As a result, the events observed in the discharge process are not completely reversible other than the de-alloying process. From the GCD

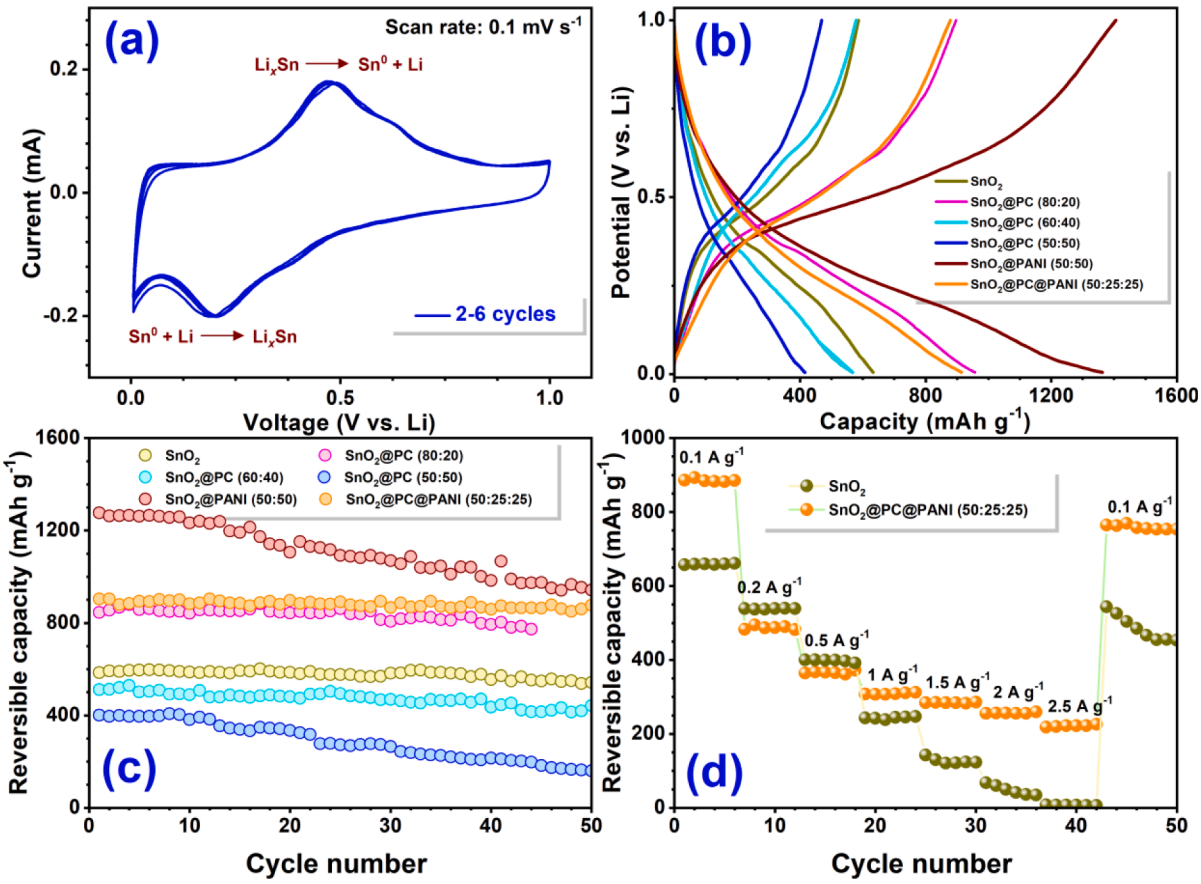

Fig. 4. Electrochemical performance of SnO_2 and SnO_2 composites in half-cell assembly with Li: (a) Cyclic voltammogram of SnO_2@PC@PANI at a scan rate of 0.1 mV s^{-1}, (b) typical galvanostatic charge-discharge profile (second cycle), (c) plot of charge capacity *vs.* cycle number, and (d) rate capability studies of SnO_2 and SnO_2@PC@PANI composite in at different current densities (0.1 to 2.5 A g^{-1}).

measurements, it is evident that the SnO_2@PC@PANI composite displays a high capacity and stable performance compared to other composites. It has an initial reversible specific capacity of ~903 mAh g^{-1} and achieved ~88% capacity retention after 50 cycles. Initially, the bare SnO_2 exhibited a better capacity when compared with the other composites. However, as the cycles progressed, the discharge capacity was reduced considerably due to the unsustainable volume variation during the alloying-dealloying reaction [23,28]. On the other hand, other composites have better cycling performance, but the specific capacity value is not up to the mark, and of course, stability as well. The extended plot of charge/reversible capacity *vs.* cycle number of all the composites is given in Fig. S4. Also, the comparison of GCD analysis (Ecell *vs.* time graph) of SnO_2 and SnO_2@PC@PANI *vs.* Li is given in Fig. S5. The presence of both PC and PANI played a vital role in sustaining the volume variation during the cycling process. The presence of more amount of PC eventually dilutes the electrical conductivity but sustains the volume variation during the alloying-dealloying process. The PANI is known for its high electrical conductivity, which provides sufficient conductivity to the composite. The reduced capacity compared to the bare SnO_2 is mainly due to the inclusion of the passive PC and PANI loading for calculation. From the given GCD profile at different current rates (Fig. 4(d)), we could see the complete dominance of SnO_2@PC@PANI over bare SnO_2 (Fig. S6) in terms of capacity retention and, thereby, cyclic reversibility. As expected, the capacity decreases with the increase in the current rate. Nevertheless, more than 93% of the capacity is regained as the current rate is again decreased to a lower current rate, which indicates the reversibility and stability of the SnO_2@PC@PANI comparing SnO_2.

The SEI layer has a primary role in the better conversion and alloying type anodes performance. The electrochemical performance can be enhanced with the stable and robust SEI layer [40–42]. Hence, *in-situ*-electrochemical impedance spectroscopy (*in-situ*-EIS) study was carried out for Li/SnO_2@PC@PANI half-cell and was recorded for the 1st, 5th, 10th, 25th, and 50th cycles (Fig. 5). We could observe an increased transfer resistance (R_{CT}) after the first cycle, primarily due to SEI layer formation causing the irreversible capacity loss. At the lower cut-off potential of 5 mV *vs.* Li, the R_{CT} values are found to be higher irrespective of the charge or discharge process due to the growth of the SEI layer. When the cell potential approaches the upper cur-off potential of 1 V *vs.* Li, a dramatic reduction in the R_{CT} is observed, which is associated with the depletion of SEI. The trend of growth and depletion of the SEI layer is continuously seen for almost all cycles. The *in-situ* impedance is direct evidence of how the SEI formation and depletion take place during the charge-discharge process. However, after the first charge-discharge, a lower and constant value of R_{CT} is noticed (at 1 V *vs.* Li), and it persisted till the 50th cycle. This led to the increased electrochemical performance of the Li/SnO_2@PC@PANI half-cell due to the stable and robust SEI layer formed. Also, an EIS was performed before cycling for the different SnO_2 composites (Fig. S7), from which we could compare the R_{CT} value of different SnO_2 composites.

The Li/PC half-cell electrochemical performance is tested in the potential window of 2 to 4.5 V *vs.* Li. The Li/PC stores charge by simple non-faradaic adsorption/desorption (physisorption) mechanism. The cations (Li^+ ions) and anions (PF_6^- ions) are adsorbed/desorbed during the charging/discharging of the cell; hence, energy storage/energy delivery takes place. The GCD analysis of the Li/PC half-cell (Fig. S8) was performed for over 180 cycles, and we could observe stable cycling performance with high capacity retention. The LIC combines two types

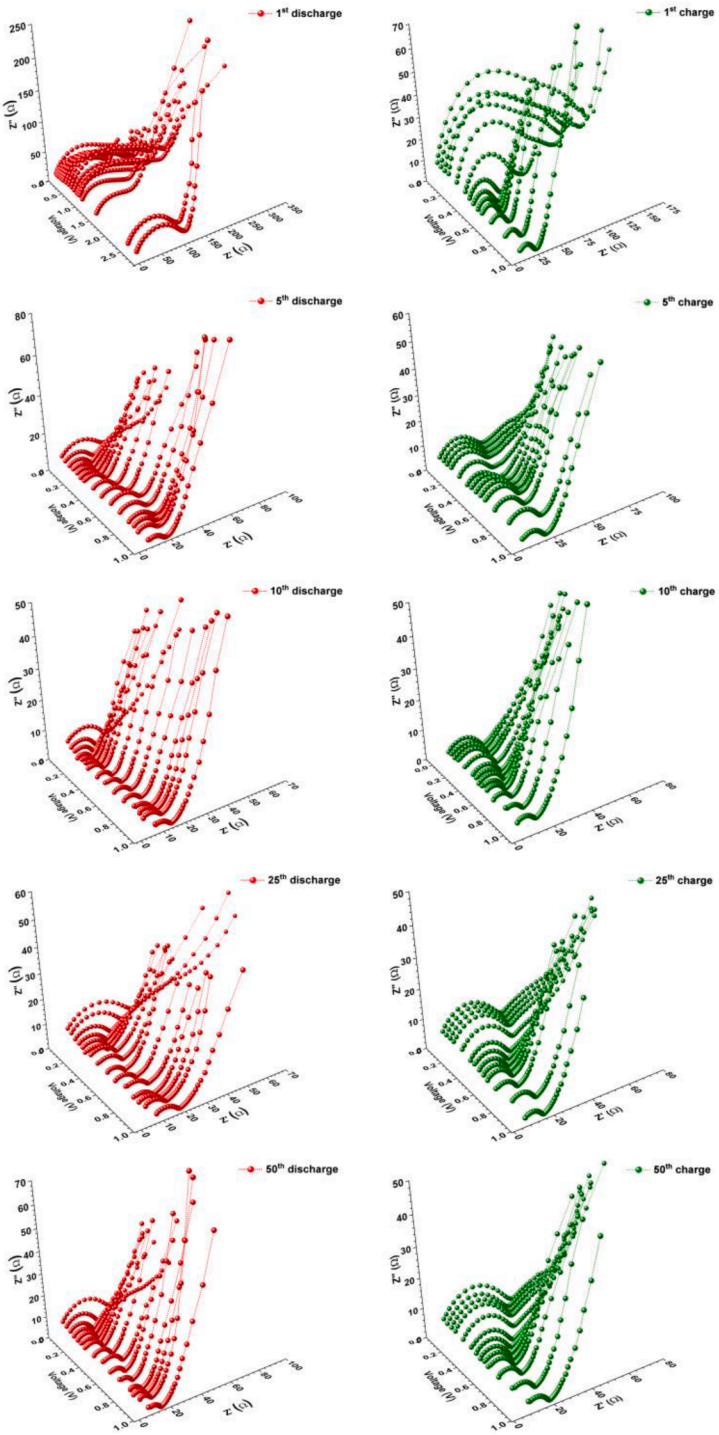

Fig. 5. An *in-situ*-electrochemical impedance spectroscopy (*in-situ*-EIS) profile of Li/SnO_2@PC@PANI half-cell. Impedance spectra of 1st, 5th, 10th, 25th, and 50th charge-discharge cycles at different potential intervals.

of electrodes with different charge storage mechanisms: A battery-type electrode with a faradaic process and a capacitive-type electrode with a non-faradaic charge storage mechanism. The faradaic process (here alloying) occurs at the anode, and the cathode has a simple adsorption/desorption reaction. As the two electrodes have different energy storage mechanisms, there occurs a kinetic mismatch between the two. Hence, it is inevitable to balance the mass to achieve higher energy density. Based on the half-cell performance of both electrodes (*vs.* Li), the charge is balanced between electrodes by the following equation.

$$M_1C_1 = M_2C_2$$

Where M_1 is the mass of SnO_2@PC@PANI, C_1 is the specific capacity of SnO_2@PC@PANI, M_2 is the mass of PC, and C_2 is the specific capacity of PC.

The PC/SnO_2@PC@PANI LIC is fabricated in such a way that, at first, the Li/SnO_2@PC@PANI half-cell is kept for GCD analysis for a few cycles and stopped at the third discharged state to obtain the lithiated phase (Li_xSn + Li_2O). After the prelithiation (Li_xSn + Li_2O) step, the half-cell is dismantled and paired with the mass-balanced PC electrode to get PC/SnO_2@PC@PANI assembly, *i.e.*, LIC. The fabricated LIC has two charge storage mechanisms: a Faradaic (alloying/de-alloying)

reaction occurs at one electrode, and a non-faradaic (adsorption/desorption) reaction occurs at another electrode. The electrochemical performance of the full-cell was tested at four different temperature conditions to study its operation under different climatic conditions. The potential *vs*. time graphs of LIC at different current rates at different temperature conditions is given in Fig. 6(a–d). From the graph, we can see that as the current rate increases, there is a decrease in the charge-storage time. This is mainly because of the insufficient time for the faradaic process to occur, and the reaction happens only at the surface instead of the bulk.

The energy density and power density of LIC at different current rates at different temperatures are compared using the Ragone plot given in Fig. 6(e). The values are calculated based on the total mass of the active material in the anode and cathode. The PC/SnO_2@PC@PANI cell exhibited its best performance at room temperature with a maximum energy density of ~175 Wh kg^{-1}, consistent with previously reported values [5]. Our PC/SnO_2@PC@PANI cell dominates over the previously reported LICs (Fig. S9) in terms of energy density and power density. In addition, superior performance has been observed when compared with the previously reported other alloy-type anodes [43–50] (Fig. S10). The LIC also rendered its better performance at different temperature conditions as well. While comparing with the low temperatures, the better performance of LIC is observed at high temperatures (50 °C). A reasonable energy density of 161.43 Wh kg^{-1} was recorded at 50 °C. The increased performance of LIC is mainly due to the increased electrolyte activity at higher temperatures. Moreover, though the energy density value of LIC at low temperatures was not up to that of room temperature, its performance was very significant. The best power density value of 7.6 kW kg^{-1} was observed at low temperatures (10 °C). The decreased Li storage performance at low temperatures is majorly related to the freezing of the liquid electrolyte. Although there is a difference in the energy and power density values, the potential drop is negligible, irrespective of the atmospheric conditions. This is one of the significances of using this composite as a battery-type electrode (Fig. 6(f)). The GCD analysis of LIC was also performed at different temperatures and is given in Fig. 6(g) with capacity normalized to 100% for easier comparison. We could see a stable and superior performance of LIC at 50 °C, which attributes to the increased conductivity at the higher temperature [43]. In general, liquid-based electrolytes exhibit inferior performance at higher temperatures due to the increased side reactions. However, in our LIC, the robustness and stability of the SEI layer (through *in-situ* EIS) promote better cyclability and increased performance at every temperature condition. Moreover, the long-term cyclic stability was also analyzed at a current rate of 1 A g^{-1} at room temperature, as shown in Fig. 6(g). The

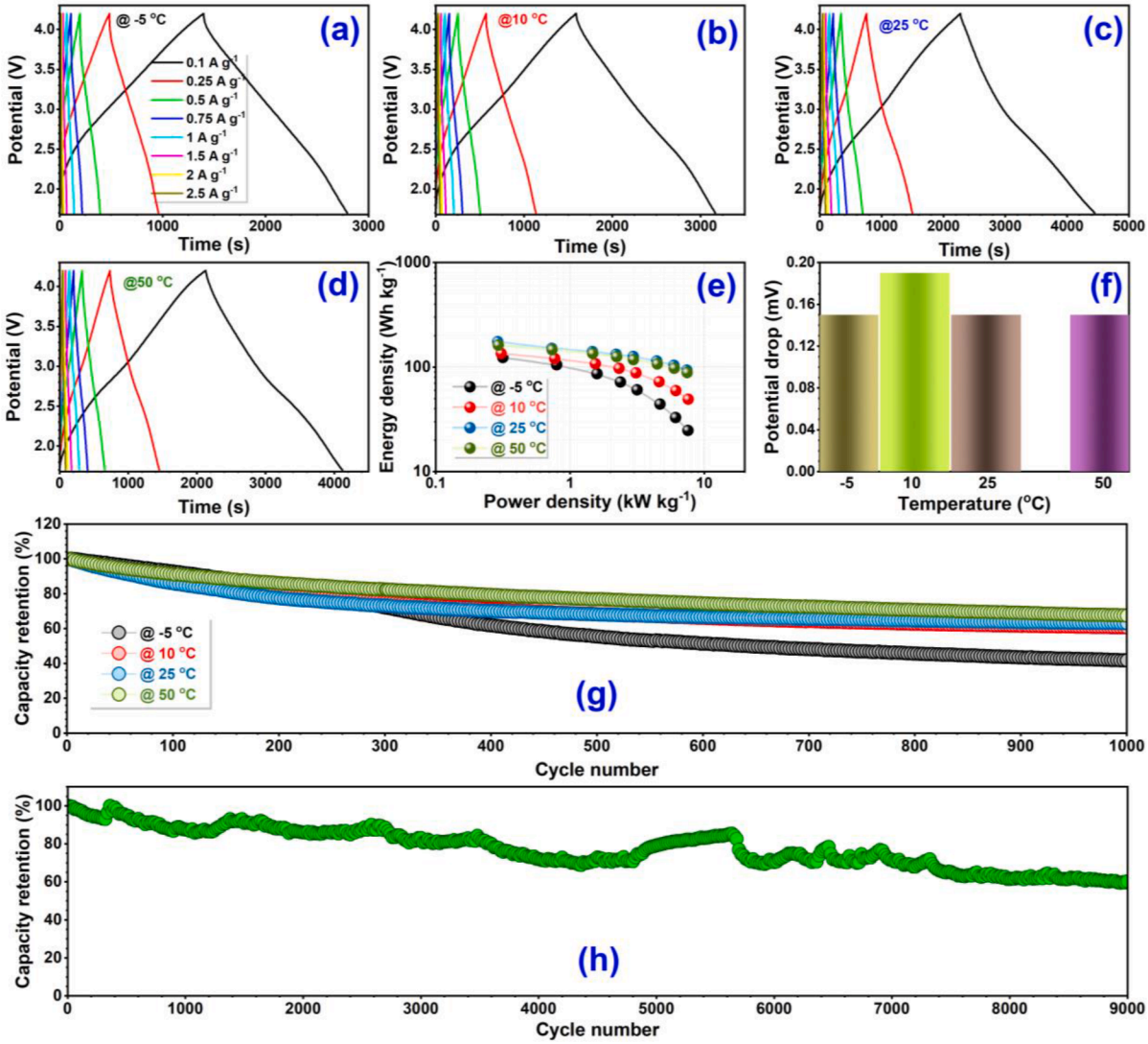

Fig. 6. Electrochemical performance of AC/SnO_2@PC@PANI LIC: (a–d) galvanostatic charge-discharge at different temperatures (−5, 10, 25, and 50 °C), (e) Ragone plot comparing energy density and power density at different temperatures, (f) potential drop *vs.* temperature plot, (g) long-term cyclic performance at different temperatures at a current density of 1 A g^{-1}, and (h) long-term cycling stability at room temperature at a current density of 1 A g^{-1}.

LIC displayed capacity retention of 79% even after 5000 cycles, which is close to the practical limitation of 80% retention. We strongly believe that the presence of polymer and activated carbon along with the redox element (SnO_2) with three-dimensional urchin-like morphology synergistically provides better electrochemical activity for the SnO_2@PC@PANI composite. On the other hand, the contribution from the palmyra fruit-derived activated carbon is also worth mentioning. Although the LIC exhibited superior electrochemical performance, further studies are in progress, especially at high current rates, to improve its energy and power density.

4. Conclusion

We designed a LIC with a battery type SnO_2@PC@PANI anode and a capacitive type PC cathode. The high surface area carbon used in both anode and cathode is derived from the palmyra fruit by carbonization, activation, and followed by devolatilization. It is then polymerized with polyaniline and made composite with synthesized hierarchical SnO_2 to use as the anode for LIC. The interfacial properties were studied using *in-situ* impedance, which substantiates the SEI layer formation process in the Li/SnO_2@PC@PANI half-cell. The PC/SnO_2@PC@PANI-based LIC delivered a maximum energy density of ~175 Wh kg^{-1} and power density of 7.42 kW kg^{-1} at room temperature. The electrochemical analysis of LIC at different temperatures was performed, and the best was observed at higher temperatures. Moreover, the long-term cyclic stability was tested, and better performance was observed even after 9000 cycles. Overall, the performance of LIC was remarkable and momentous; further studies are in progress to improve the performance of SnO_2 as an anode for LIC.

CRediT authorship contribution statement

Manohar Akshay: Conceptualization, Formal analysis, Validation, Writing – original draft, Writing – review & editing. **Selvarasu Praneetha:** Conceptualization, Formal analysis, Validation. **Yun-Sung Lee:** Formal analysis, Validation, Writing – original draft, Writing – review & editing. **Vanchiappan Aravindan:** Conceptualization, Formal analysis, Validation, Writing – original draft, Writing – review & editing.

Declaration of Competing Interest

The authors declare that they have no known competing financial interests or personal relationships that could have appeared to influence the work reported in this paper.

Acknowledgments

YSL acknowledges the financial support from the National Research Foundation of Korea (NRF) grant funded by the Korean government (Ministry of Science, ICT&Future Planning) (No. 2019R1-A2C1007620). VA acknowledges financial support from the Science and Engineering Research Board (SERB), a statutory body of the Department of Science and Technology, Govt. of India, through Start-up Research Grant (SRG/2020/000002) and Swarnajayanti Fellowship (SB/SJF/2020-21/12).

Supplementary materials

Supplementary material associated with this article can be found, in the online version, at doi:10.1016/j.electacta.2022.141599.

References

[1] M. Soltani, S.H. Beheshti, A comprehensive review of lithium ion capacitor: development, modelling, thermal management and applications, J. Energy Storage 34 (2021), 102019, https://doi.org/10.1016/j.est.2020.102019.
[2] N. Omar, J. Ronsmans, Y. Firozu, M.A. Monem, A. Samba, H. Gualous, O. Hegazy, J. Smekens, T. Coosemans, P. Van Den Bossche, J. Van Mierlo, Lithium-ion capacitor - Advanced technology for rechargeable energy storage systems, 2013, in: Proceedings of the World Electric Vehicle Symposium and Exhibition (EVS27) 2014, 2014, pp. 1–11, https://doi.org/10.1109/EVS.2013.6914718.
[3] P. Naskar, D. Kundu, A. Maiti, P. Chakraborty, B. Biswas, A. Banerjee, Frontiers in hybrid ion capacitors: a review on advanced materials and emerging devices, ChemElectroChem 8 (2021) 1393–1429, https://doi.org/10.1002/celc.202100029.
[4] D.P. Dubal, O. Ayyad, V. Ruiz, P. Gómez-Romero, Hybrid energy storage: the merging of battery and supercapacitor chemistries, Chem. Soc. Rev. 44 (2015) 1777–1790, https://doi.org/10.1039/c4cs00266k.
[5] V. Aravindan, Y.S. Lee, Building next-generation li-ion capacitors with high energy: an approach beyond intercalation, J. Phys. Chem. Lett. 9 (2018) 3946–3958, https://doi.org/10.1021/acs.jpclett.8b01386.
[6] A. Muzaffar, M.B. Ahamed, K. Deshmukh, J. Thirumalai, A review on recent advances in hybrid supercapacitors: design, fabrication and applications, Renew. Sustain. Energy Rev. 101 (2019) 123–145, https://doi.org/10.1016/j.rser.2018.10.026.
[7] Y. An, T. Liu, C. Li, X. Zhang, T. Hu, X. Sun, K. Wang, C. Wang, Y. Ma, A general route for the mass production of graphene-enhanced carbon composites toward practical pouch lithium-ion capacitors, J. Mater. Chem. A 9 (2021) 15654–15664, https://doi.org/10.1039/D1TA03933D.
[8] J. Huang, J. Chen, L. Ma, Q. Liu, M. Wang, L. Liao, T. Rujiralai, L. Xu, In-situ coupling SnS with nitrogen-doped porous carbon for boosting Li-storage in lithium-ion battery and capacitor, Electrochim. Acta. 365 (2021), 137350, https://doi.org/10.1016/j.electacta.2020.137350.
[9] X. Huang, W. Zhou, X. Chen, C. Jiang, Z. Zou, High performance Li-ion hybrid capacitors with micro-sized $Nb_{14}W_3O_{44}$ as anode, Electrochim. Acta 368 (2021), 137613, https://doi.org/10.1016/j.electacta.2020.137613.
[10] B. Krüner, C. Odenwald, N. Jäckel, A. Tolosa, G. Kickelbick, V. Presser, Silicon oxycarbide beads from continuously produced polysilsesquioxane as stable anode material for lithium-ion batteries, ACS Appl. Energy Mater. 1 (2018) 2961–2970, https://doi.org/10.1021/acsaem.8b00716.
[11] B. Li, H. Hu, H. Hu, C. Huang, D. Kong, Y. Li, Q. Xue, Z. Yan, W. Xing, X. Gao, Improving the performance of lithium ion capacitor by stabilizing anode working potential using $CoSe_2$ nanoparticles embedded nitrogen-doped hard carbon microspheres, Electrochim. Acta 370 (2021), 137717, https://doi.org/10.1016/j.electacta.2021.137717.
[12] W. Liu, X. Zhang, Y. Xu, L. Wang, Z. Li, C. Li, K. Wang, X. Sun, Y. An, Z.S. Wu, Y. Ma, 2D graphene/MnO heterostructure with strongly stable interface enabling high-performance flexible solid-state lithium-ion capacitors, Adv. Funct. Mater. 32 (2022), 2202342, https://doi.org/10.1002/adfm.202202342.
[13] Z. Vasiljević, M.P. Dojčinović, J.D. Vujančević, M. Spreitzer, J. Kovač, D. Bartolić, S. Marković, I. Janković-Častvan, N.B. Tadić, M.V. Nikolić, Exploring the impact of calcination parameters on the crystal structure, morphology, and optical properties of electrospun Fe_2TiO_5nanofibers, RSC Adv. 11 (2021) 32358–32368, https://doi.org/10.1039/d1ra05748k.
[14] L. Zhao, H.H. Wu, C. Yang, Q. Zhang, G. Zhong, Z. Zheng, H. Chen, J. Wang, K. He, B. Wang, T. Zhu, X.C. Zeng, M. Liu, M.S. Wang, Mechanistic origin of the high performance of Yolk@Shell Bi_2S_3@N-doped carbon nanowire electrodes, ACS Nano 12 (2018) 12597–12611, https://doi.org/10.1021/acsnano.8b07319.
[15] F. Li, Y. Li, L. Zhao, J. Liu, F. Zuo, F. Gu, H. Liu, R. Liu, Y. Li, J. Zhan, Q. Li, H. Li, Revealing an intercalation-conversion-heterogeneity hybrid lithium-ion storage mechanism in transition metal nitrides electrodes with jointly fast charging capability and high energy output, Adv. Sci. 9 (2022), 2203895, https://doi.org/10.1002/advs.202203895.
[16] M. Akshay, K. Subramanyan, M.L. Divya, Y.S. Lee, V. Aravindan, Choice of binder on conversion type CuO nanoparticles toward building high energy Li-ion capacitors: an approach beyond intercalation, Adv. Mater. Technol. 7 (2022), 2200423, https://doi.org/10.1002/admt.202200423.
[17] Z. Zhen, M. Jin, L. Caina, M. Wei, L. Yu, Epitaxial growth of SnO_2 films on 6H-SiC (0 0 0 1) by MOCVD, Mater. Res. Bull. 47 (2012) 253–256, https://doi.org/10.1016/j.materresbull.2011.11.034.
[18] K. Subramanyan, M. Akshay, Y.S. Lee, V. Aravindan, Fabrication of Na-Ion full-cells using carbon-coated $Na_3V_2(PO_4)_2O_2F$ cathode with conversion type CuO nanoparticles from spent Li-ion batteries, Small Methods 6 (2022), 2200257, https://doi.org/10.1002/smtd.202200257.
[19] Q. Li, H. Li, Q. Xia, Z. Hu, Y. Zhu, S. Yan, C. Ge, Q. Zhang, X. Wang, X. Shang, S. Fan, Y. Long, L. Gu, G.X. Miao, G. Yu, J.S. Moodera, Extra storage capacity in transition metal oxide lithium-ion batteries revealed by *in situ* magnetometry, Nat. Mater. 20 (2021) 76–83, https://doi.org/10.1038/s41563-020-0756-y.
[20] H. Li, Z. Hu, Q. Xia, H. Zhang, Z. Li, H. Wang, X. Li, F. Zuo, F. Zhang, X. Wang, W. Ye, Q. Li, Y. Long, Q. Li, S. Yan, X. Liu, X. Zhang, G. Yu, G.X. Miao, Operando magnetometry probing the charge storage mechanism of CoO lithium-ion batteries, Adv. Mater. 33 (2021), 2006629, https://doi.org/10.1002/adma.202006629.
[21] W.J. Zhang, A review of the electrochemical performance of alloy anodes for lithium-ion batteries, J. Power Sources. 196 (2011) 13–24, https://doi.org/10.1016/j.jpowsour.2010.07.020.
[22] X. Wang, T. Zheng, Y.J. Cheng, S. Yin, Y. Xia, Q. Ji, Z. Xu, S. Liang, L. Ma, X. Zuo, J. Q. Meng, J. Zhu, P. Müller-Buschbaum, SnO_2/Sn/Carbon nanohybrid lithium-ion battery anode with high reversible capacity and excellent cyclic stability, Nano Sel. 2 (2021) 642–653, https://doi.org/10.1002/nano.202000213.
[23] V. Aravindan, K.B. Jinesh, R.R. Prabhakar, V.S. Kale, S. Madhavi, Atomic layer deposited (ALD) SnO_2 anodes with exceptional cycleability for Li-ion batteries, Nano Energy 2 (2013) 720–725.
[24] Y. Wang, Z.X. Huang, Y. Shi, J.I. Wong, M. Ding, H.Y. Yang, Designed hybrid nanostructure with catalytic effect: beyond the theoretical capacity of SnO_2 anode

material for lithium ion batteries, Sci. Rep. 5 (2015) 9164, https://doi.org/10.1038/srep09164.
[25] M.V. Reddy, G.V. Subba Rao, B.V.R. Chowdari, Metal oxides and oxysalts as anode materials for Li ion batteries, Chem. Rev. 113 (2013) 5364–5457, https://doi.org/10.1021/cr3001884.
[26] Z. Wen, Q. Wang, Q. Zhang, J. Li, *In situ* growth of mesoporous SnO_2 on multiwalled carbon nanotubes: a novel composite with porous-tube structure as anode for lithium batteries, Adv. Funct. Mater. 17 (2007) 2772–2778, https://doi.org/10.1002/adfm.200600739.
[27] L. Zhang, H. Bin Wu, B. Liu, X.W. (David) Lou, Formation of porous SnO_2 microboxes via selective leaching for highly reversible lithium storage, Energy Environ. Sci. 7 (2014) 1013–1017, https://doi.org/10.1039/C3EE43305F.
[28] V. Aravindan, J. Sundaramurthy, E.N. Kumar, P.S. Kumar, W.C. Ling, R. von Hagen, S. Mathur, S. Ramakrishna, S. Madhavi, Does carbon coating really improves the electrochemical performance of electrospun SnO_2 anodes? Electrochim. Acta. 121 (2014) 109–115, https://doi.org/10.1016/j.electacta.2013.12.141.
[29] P. Sennu, V. Aravindan, Y.S. Lee, Marine algae inspired pre-treated SnO_2 nanorods bundle as negative electrode for Li-ion capacitor and battery: an approach beyond intercalation, Chem. Eng. J. 324 (2017) 26–34, https://doi.org/10.1016/j.cej.2017.05.003.
[30] B.P. Vinayan, S. Ramaprabhu, Facile synthesis of SnO_2 nanoparticles dispersed nitrogen doped graphene anode material for ultrahigh capacity lithium ion battery applications, J. Mater. Chem. A 1 (2013) 3865–3871, https://doi.org/10.1039/C3TA01515G.
[31] H. Wang, J. Lin, Z.X. Shen, Polyaniline (PANi) based electrode materials for energy storage and conversion, J. Sci. Adv. Mater. Devices 1 (2016) 225–255, https://doi.org/10.1016/j.jsamd.2016.08.001.
[32] M. Arnaiz, C. Botas, D. Carriazo, R. Mysyk, F. Mijangos, T. Rojo, J. Ajuria, E. Goikolea, Reduced graphene oxide decorated with SnO_2 nanoparticles as negative electrode for lithium ion capacitors, Electrochim. Acta 284 (2018) 542–550, https://doi.org/10.1016/j.electacta.2018.07.189.
[33] C. Liu, Z. He, J. Niu, Q. Cheng, Z. Zhao, H. Li, J. Shi, H. Wang, Two-dimensional SnO_2anchored biomass-derived carbon nanosheet anode for high-performance Li-ion capacitors, RSC Adv. 11 (2021) 10018–10026, https://doi.org/10.1039/d1ra00822f.
[34] Z. Lu, K. Zou, K. Liang, Y. Deng, G. Chen, Integrating N-doped porous carbon-encapsulated ultrafine $SnO_2$with MXene nanosheets via electrostatic self-assembly as a superior anode material for lithium ion capacitors, ACS Appl. Energy Mater. 5 (2022) 8198–8210, https://doi.org/10.1021/acsaem.2c00746.
[35] X. Zhou, Z. Geng, B. Li, C. Zhang, Oxygen doped activated carbon/SnO_2 nanohybrid for high performance lithium-ion capacitor, J. Electroanal. Chem. 850 (2019), 113398, https://doi.org/10.1016/j.jelechem.2019.113398.
[36] M.L. Divya, S. Praneetha, Y.S. Lee, V. Aravindan, Next-generation Li-ion capacitor with high energy and high power by limiting alloying-intercalation process using SnO_2@Graphite composite as battery type electrode, Compos. Part B Eng. 230 (2022), 109487, https://doi.org/10.1016/j.compositesb.2021.109487.
[37] J. Zhang, X. Liu, S. Wu, M. Xu, X. Guo, S. Wang, Au nanoparticle-decorated porous SnO_2 hollow spheres: a new model for a chemical sensor, J. Mater. Chem. 20 (2010) 6453–6459, https://doi.org/10.1039/C0JM00457J.
[38] X. Han, R. Li, S. Qiu, X. Zhang, Q. Zhang, Y. Yang, Sonochemistry-enabled uniform coupling of SnO_2 nanocrystals with graphene sheets as anode materials for lithium-ion batteries, RSC Adv. 9 (2019) 5942–5947, https://doi.org/10.1039/C9RA00554D.
[39] Y. Cheng, J. Huang, H. Qi, L. Cao, J. Yang, Q. Xi, X. Luo, K. Yanagisawa, J. Li, Adjusting the chemical bonding of SnO_2@CNT composite for enhanced conversion reaction kinetics, Small 13 (2017), 1700656, https://doi.org/10.1002/smll.201700656.
[40] X.B. Cheng, R. Zhang, C.Z. Zhao, F. Wei, J.G. Zhang, Q. Zhang, A review of solid electrolyte interphases on lithium metal anode, Adv. Sci. 3 (2016), 1500213, https://doi.org/10.1002/advs.201500213.
[41] S. Menkin, D. Golodnitsky, E. Peled, Artificial solid-electrolyte interphase (SEI) for improved cycleability and safety of lithium–ion cells for EV applications, Electrochem. Commun. 11 (2009) 1789–1791, https://doi.org/10.1016/j.elecom.2009.07.019.
[42] J.B. Goodenough, P. Singh, Review—solid electrolytes in rechargeable electrochemical cells, J. Electrochem. Soc. 162 (2015) A2387–A2392, https://doi.org/10.1149/2.0021514jes.
[43] S. Natarajan, Y.S. Lee, V. Aravindan, Biomass-derived carbon materials as prospective electrodes for high-energy lithium- and sodium-ion capacitors, Chem. Asian J. 14 (2019) 936–951, https://doi.org/10.1002/asia.201900030.
[44] S. Jayaraman, G. Singh, S. Madhavi, V. Aravindan, Elongated graphitic hollow nanofibers from vegetable oil as prospective insertion host for constructing advanced high energy Li-ion capacitor and battery, Carbon 134 (2018) 9–14, https://doi.org/10.1016/j.carbon.2018.03.065. N. Y.
[45] S. Jayaraman, S. Madhavi, V. Aravindan, High energy Li-ion capacitor and battery using graphitic carbon spheres as an insertion host from cooking oil, J. Mater. Chem. A. 6 (2018) 3242–3248, https://doi.org/10.1039/c7ta09905c.
[46] S. Jayaraman, A. Jain, M. Ulaganathan, E. Edison, M.P. Srinivasan, R. Balasubramanian, V. Aravindan, S. Madhavi, Li-ion vs. Na-ion capacitors: a performance evaluation with coconut shell derived mesoporous carbon and natural plant based hard carbon, Chem. Eng. J. 316 (2017) 506–513, https://doi.org/10.1016/j.cej.2017.01.108.
[47] P. Sennu, V. Aravindan, M. Ganesan, Y.G. Lee, Y.S. Lee, Biomass-derived electrode for next generation lithium-ion capacitors, ChemSusChem 9 (2016) 849–854, https://doi.org/10.1002/cssc.201501621.
[48] X. Liu, H.G. Jung, S.O. Kim, H.S. Choi, S. Lee, J.H. Moon, J.K. Lee, Silicon/copper dome-patterned electrodes for high-performance hybrid supercapacitors, Sci. Rep. 3 (2013) 3183, https://doi.org/10.1038/srep03183.
[49] R. Yi, S. Chen, J. Song, M.L. Gordin, A. Manivannan, D. Wang, High-performance hybrid supercapacitor enabled by a high-rate Si-based anode, Adv. Funct. Mater. 24 (2014) 7433–7439, https://doi.org/10.1002/adfm.201402398.
[50] J. Luo, W. Zhang, H. Yuan, C. Jin, L. Zhang, H. Huang, C. Liang, Y. Xia, J. Zhang, Y. Gan, X. Tao, Pillared structure design of MXene with ultralarge interlayer spacing for high-performance lithium-ion capacitors, ACS Nano 11 (2017) 2459–2469, https://doi.org/10.1021/acsnano.6b07668.